TECHNICAL ARTICLE

Effects of Extrusion Ratio on the Microstructure, Texture and Mechanical Properties of Mg-2.5Nd-0.5Zn-0.5Zr Alloy Sheets

Songhui Wang, Jinqi Pan, Wenzhuo Xie, Jianlei Yang, Wencong Zhang, and Wenzhen Chen

The effects of different extrusion ratios (7.6, 12.5 and 26.1) on the microstructure evolution, texture characteristics and mechanical properties of Mg-2.5Nd-0.5Zn-0.5Zr (wt.%) alloys have been systematically studied. The results showed that with the increase of extrusion ratio, the dynamic recrystallization grain size decreased first and then increased, the texture state changed from weakened bimodal texture to strong basal texture with the texture strength increased from 6.7 to 19.4. The growth of grain size was mainly attributed to rise of temperature transformed by the deformation heat with high extrusion ratio and the more intense extrusion deformation. The mechanical properties of the alloy increased first and then decreased with the increase of the extrusion ratio. When the extrusion ratio was 12.5, the alloy exhibited excellent mechanical properties. The higher yield strength results from the interaction of refinement strengthening, dislocation strengthening, precipitation strengthening and texture strengthening. With the increase of extrusion ratio, the proportion of basal slip increased gradually when the alloy was tensile in extrusion direction, and the deformation mechanism was mainly basal slip. When the alloy was tensile along the transverse direction, the proportion of basal slip decreased, and the proportion of prismatic slip increased gradually. The main deformation mechanism were basal slip and prismatic slip.

1. Introduction

Mg alloys has become a research hotspot in recent decades due to its advantages of low density, high specific strength, stiffness and electronic shielding performance (Ref 1, 2). However, its low strength and poor machinability greatly limited its commercial use (Ref 3, 4). Up to now, there were many feasible methods to improve the strength and plasticity of Mg alloys, such as alloying and severe plastic deformation (Ref 5-8). Typically, the addition of rare-earth elements (e.g., Gd, Y, Nd, Sm, Ce, Sc, Er, Yb, etc.) could significantly improve the strength and plasticity of Mg alloys (Ref 3-6, 9, 10). Specifically, Lv et al. (Ref 11) successfully developed Mg-Zn-Zr alloy with excellent strength ($\sim$ 370 MPa) and plasticity ($\sim$ 25.9%) through alloying (Yb) + hot extrusion process. Among them, Yb plays an important role in the microstructure regulation of the Mg-Zn-Zr alloy. Similarly, Lyu et al. (Ref 12) successfully developed high strength ($\sim$ 465 MPa) Mg-Zn-Zr alloy by alloying (Y/Sm) + hot extrusion process. Additionally,

Xu et al. (Ref 8) successfully prepared the AM60 Mg alloy sheets with ultra-fine lamellar structure through high strain rate rolling, which made the AM60 Mg alloy sheet have good strength and plasticity.

Nd element was one of the lighter rare earth elements and has a higher solubility (3.6 wt. %) at eutectic temperature (545 °C) (Ref 13-15). It has remarkable effect of aging precipitation strengthening (Ref 16, 17). In recent years, Mg-Nd-Zn-Zr alloy was favored by researchers because of its low rare earth content and excellent properties (Ref 13-15). To date, the research about Mg-Nd-Zn-Zr alloy mainly focuses on the effect of heat treatment on the precipitation sequence and mechanical properties (Ref 13-17). However, studies on the effect of plastic deformation on Mg-Nd-Zn-Zr alloys were relatively backward, and plastic deformation was beneficial to both the strength and plasticity of the alloys. For example, casting Mg-Nd-based alloys usually exhibit coarse-grain characteristics ($\sim$ 100 μm), severe dendrite segregation, low load carrying strength ($\sim$ 200 MPa) and poor plasticity ($\sim$ 10%), etc. (Ref 13-15), which greatly limit their widespread use. Therefore, refining the grain size and improving the strength and plasticity of the Mg-Nd-Zn-Zr alloy has become a meaningful topic. Hot extrusion was an efficient and economical method to process wrought Mg alloys, which could effectively improve the mechanical properties of Mg alloys by eliminating casting defects and refining the microstructure (Ref 10). As was known to all, in the process of hot extrusion deformation, dynamic recrystallization could effectively refine grains and improve the uniformity of microstructure (Ref 18, 19). However, extrusion parameters, especially extrusion ratio (ER), have a significant impact on the microstructure evolution of Mg alloy, resulting in different grain size distribution,

Songhui Wang, Jinqi Pan, Wenzhuo Xie, Jianlei Yang, Wencong Zhang, and **Wenzhen Chen**, School of Materials Science and Engineering, Harbin Institute of Technology, Harbin 150001, People's Republic of China. Contact e-mail: zhangwencong@hit.edu.cn.

dynamic recrystallization degree, texture state and precipitated phase size, which have a significant impact on the mechanical properties of Mg alloy (Ref 20, 21). For example, Hagihara and Yu et al. (Ref 18, 22) study showed that extrusion temperature and ER affect the microstructure of the alloy, thus determined the mechanical properties of the alloy. Zhang et al. (Ref 10) found that the increase of ER led to the increase of dynamic recrystallization fraction of Mg-Sm alloy, the size of dynamic recrystallization increases, and the texture of basal was weakened, led to the decrease of strength and improvement in plasticity of the alloy. Additionally, Tang et al. (Ref 23) found that in the extrusion deformation process of AZ31 Mg alloy, the effect of ER on grain refinement was more significant than that of extrusion speed. In our previous work, it was found that the damping property of Mg-Nd-Zn-Zr alloy was significantly affected by the ER, and the damping property of the alloy decreased with the increase of the ER (Ref 24). Consequently, it was of great meaning to study the effect of ER on the microstructure evolution, texture and mechanical properties of Mg-Nd-Zn-Zr alloy to expand the application market of Mg alloys.

In this work, the effect of different extrusion ratios on the microstructure and mechanical properties of the Mg-2.5Nd-0.5Zn-0.5Zr alloy sheets was studied, and the microstructure evolution was discussed. Meanwhile, the strengthening mechanism and deformation mechanism was also analyzed.

2. Experimental Procedures

The initial alloy was Mg-2.5Nd-0.5Zn-0.5Zr (wt.%) rod (Φ100 and Φ80 mm). First, the initial alloy was solution-treated at 530 °C for 9 h. Subsequently, the alloy was preheated at 400 °C for 4 h and then extruded to sheet at 400 °C followed by air cool. More specifically, the die-exit speed was $1.0 \sim 1.5$ mm/s and the ERs was 7.6, 12.5 and 26.1, respectively. The sheets obtained by different ERs were denoted as HE1, HE2 and HE3, respectively. The extruded sheets sizes were $10 \times 100 \times 2000$ mm (HE1), $5 \times 80 \times 2000$ mm (HE2) and $3 \times 100 \times 2000$ mm (HE3), respectively. Microstructure characteristics was analyzed by scanning electron microscope (SEM), electron backscatter diffraction (EBSD) and transmission electron microscope (Talos F200S G2 TEM). The orientation imaging microscopy software of TSL OIM Analysis 7.2 was utilized for data analysis. The XRD analysis was conducted on a Smart lab x-ray diffractometer at 40 kV with Cu Kα radiation. The step size, the scanning speed and the diffraction angle (2θ) range of XRD were 0.02°, 1°/min and 10-90°, respectively. The TEM samples were ground to 40 μm size and punched into a 3-mm disk using a hole punch. Then the transmitted samples were thinned by PIPS II Model 695 Gatan with cooling system by liquid nitrogen ($-$ 120 °C). The EBSD samples were first prepared by mechanical polishing and then electropolished (5:3 C_2H_5OH and H_3PO_4 electrolyte, electropolishing for 2 min at 0.5 A and 5 min at 0.25 A). Tension tests were carried out on Instron 5967 with a strain rate of 1×10^{-3} s^{-1} at room temperature. Tension samples were sectioned from the as-extruded sheets in two directions (the extrusion direction (ED) and the transverse direction (TD)), and the dimension of the specimens were $15 \times 4.0 \times 2.0$ mm.

3. Results and Discussion

3.1 Microstructure of Initial Alloy

Figure 1 shows the microstructure characteristics of the initial alloy. The initial alloy was approximately coarse equiaxed grain with a normal distribution (average grain size, 23.8 μm). In Fig. 1(a), many divorced eutectic phases precipitated along grain boundaries in a continuous network distributed. In order to ascertain the second phase, the XRD, TEM and EDS results are shown in Fig. 1(b-i). Clearly, the XRD results in Fig. 1(b) demonstrated that besides the magnesium matrix, there existed many intensity peaks corresponding to the $Mg_{12}Nd$ phase according to the standard spectra (Ref 4, 13). Furthermore, the TEM bright field image (Fig. 1c) and the corresponding selected area electron diffraction (SAED) pattern (Fig. 1h) and corresponding EDS maps (Fig. 1d-g). The corresponding EDS maps of Nd, Zn and Zr demonstrated that Nd and Zn were concentrated at grain boundaries, while Zr approximately equally distribute. Accordingly, this second phase was identified as the $Mg_{12}Nd$ phase (Ref 14, 24). In addition, the TEM-EDX results of the second phase (Fig. 1i) exhibited high fraction of Magnesium atoms with 85.4 wt.% and relatively high fraction of neodymium atoms with 11.82 wt.% in the second phase. This was consistent with the chemical composition of $Mg_{12}Nd$ phase. These results fully indicated that the second phase in this work was the $Mg_{12}Nd$ phase. The pole figure showed obvious diffuse property and no evident texture characteristics.

3.2 Microstructure of As-Extruded Sheets

Figure 2 presents the SEM and EDS mapping micrographs of the extruded alloy sheets. The average size and volume fraction of the second phase were measured by the Image-Pro Plus 6.0 software as shown in Table 1. As can be seen from Fig. 2, there were many discontinuous broken second phases (the red rectangle was shown by the dotted line) in HE1 alloy distributed along the ED, and the size and morphology of the second phase were significantly different. The average grain size was 2.0 ± 0.12 μm and the volume fraction was 5.25%. The corresponding mapping showed that Nd element accumulated along the ED while Zn and Zr were evenly distributed in the α-Mg matrix. The second phase of the HE2 alloy was uniformly distributed in the α-Mg matrix. In the corresponding mapping micrographs, Nd, Zn and Zr were uniformly distributed in the α-Mg matrix. The average size of the second phase was 0.98 ± 0.26 μm, and the volume fraction was 8.79%. A small amount of the second phase in HE3 alloy was distributed along the ED, and the fragmentation of the second phase could be clearly seen in the green magnified area, which was similar to that of the HE1. A small amount of Nd element accumulated in the ED, and Zn and Zr were evenly distributed in the α-Mg matrix. The average size was 1.2 ± 0.18 μm and the volume fraction was 6.93%. Compared with the initial alloy, the second phase with mesh distribution was crushed and fractured after extrusion deformation, and the coarse second phase almost disappeared. The morphology and size change of the second phase were related to the extrusion deformation (Ref 4, 21). The decrease of average size may be due to the increase of ER, the more severe deformation, and the more obvious fragmentation of the second phase. The size of the second phase in HE3 alloy was slightly larger than that of HE2 alloy,
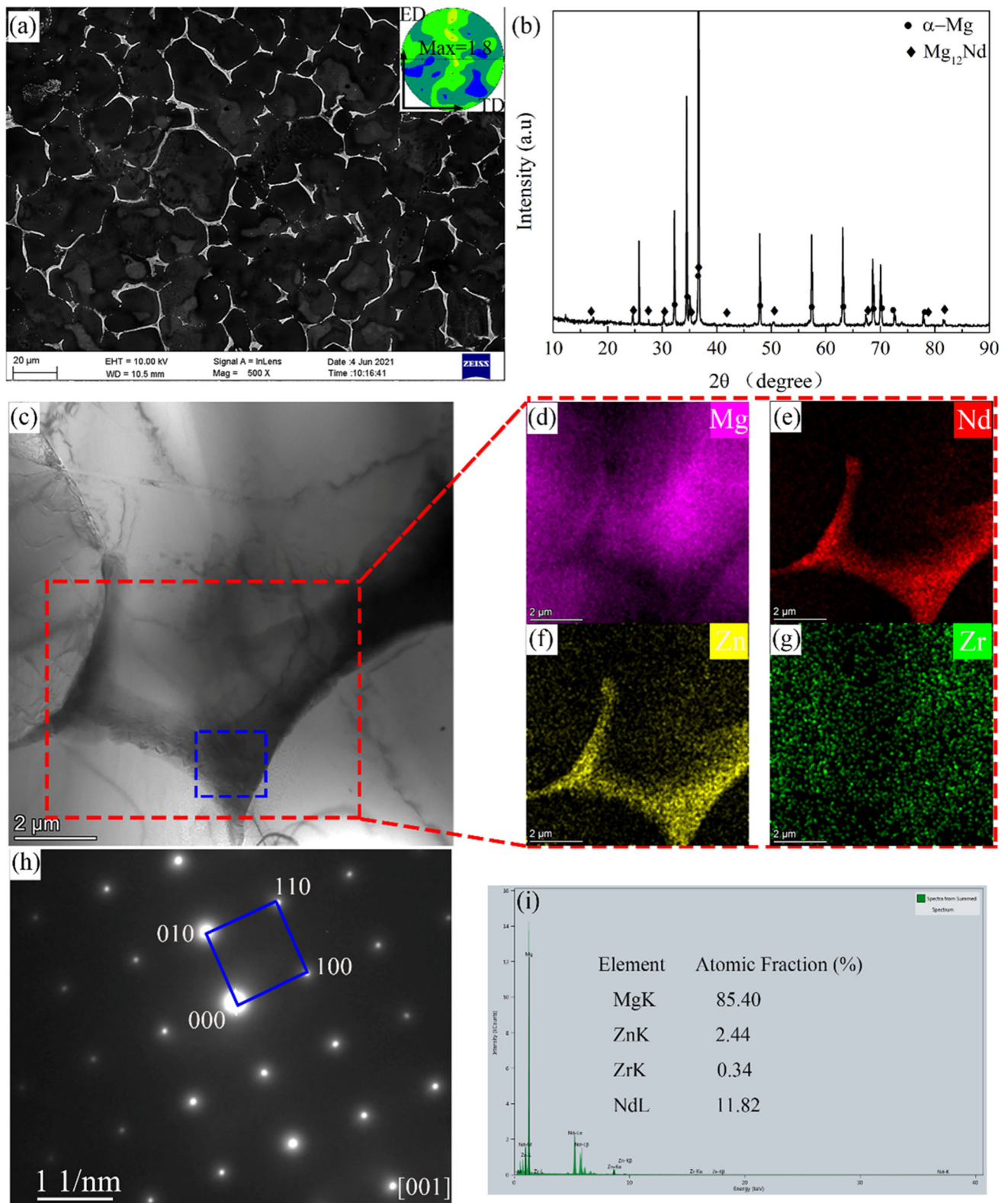
Fig. 1 Microstructures of the initial alloy: (a) Backscatter SEM image, (b) XRD pattern, (c) bright field TEM image along with the corresponding EDS mappings (d-g) of the area highlighted by a red box and the corresponding selected area electron diffraction (SAED) pattern (h) and corresponding EDX maps (i) of the area highlighted by a blue box (Color figure online)

which may be due to the increase of ER, which generates a lot of deformation heat and led to the coarsening of the second phase. And the decrease of the volume fraction may be attributed to the excessive deformation heat in the deformation process, which was not timely dispersed, and the Nd element was dissolved back into the Mg matrix. Figure 3 shows XRD
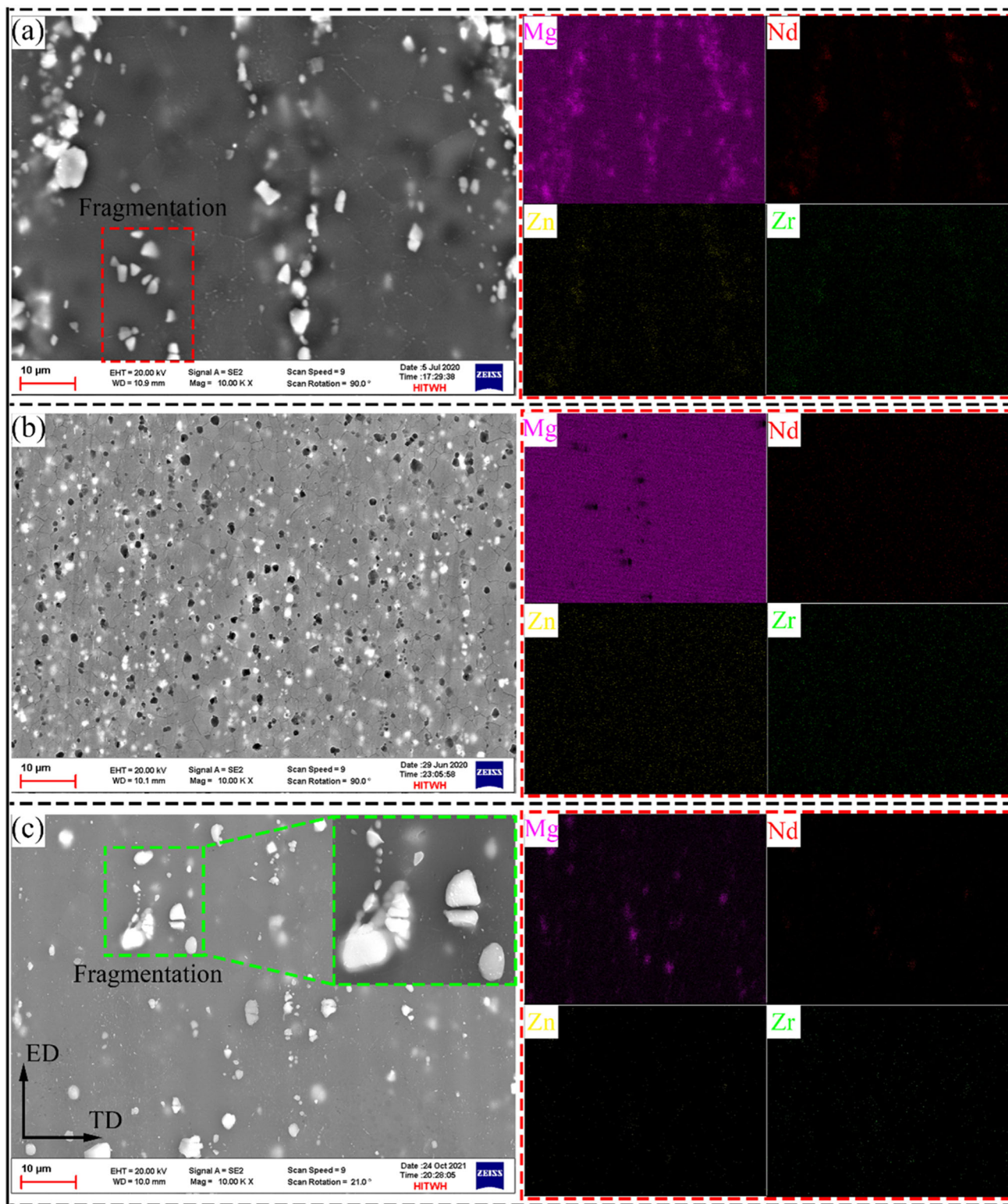
Fig. 2 SEM images and corresponding elemental mappings of the Mg-2.5Nd-0.5Zn-0.5Zr alloy sheets, (a) HE1, (b) HE2, (c) HE3

phase analysis of the extruded sheets with different ERs. Clearly, there were diffraction peaks of α-Mg and β-Mg$_{12}$Nd (PDF Card No: 1523592) in the extruded alloy sheets. The lattice constant of β-Mg$_{12}$Nd were a = 10.31 Å, c = 5.93 Å by XRD analyzed. This was consistent with the reported literature (Ref [16], [17]).

Figure 4 exhibits the TEM micrographs of the extruded alloy sheets. Clearly, the coarse second phase was broken into small second phase after extrusion deformation, and the analysis results of this SEM images were consistent. In addition, fine second phase pining at grain boundaries hindered grain boundary migration and increased nucleation rate of

dynamic recrystallization, resulting in grain refinement (Ref 4, 25). In general, Mg alloys containing the second phase, the fine dispersed second phase could pin grain boundaries and delay recrystallization. However, the larger second phase (> 1 μm) tended to be the nucleation point for recrystallization, which was conducive to promoting the recrystallization behavior, and this recrystallization mechanism was generally called particle-stimulated nucleation (PSN) (Ref 26, 27).

Table 1 Average size and volume fraction of the second phase particles of the extruded Mg-2.5Nd-0.5Zn-0.5Zr alloy sheets in different conditions

Conditions	Average size, μm	Volume fraction, %
HE1	2.0 ± 0.12	5.25 ± 0.36
HE2	0.98 ± 0.26	8.79 ± 0.22
HE3	1.2 ± 0.08	6.93 ± 0.35

Figure 5 depicts the microstructure characteristics evolution of the alloy during hot-extruded processes. In this study, the recrystallized grains with a grain average misorientation (GAM) value less than 1.2° and deformed grains with a GAM value greater than 1.2° were defined (Ref 28). As can be seen from the figure, dynamic recrystallization took place in the extrusion deformation process of the alloy, grain was significantly refined, and the microstructure uniformity of the sheet was expressively improved (Ref 18-20). With the increase of ER, the average grain size of the alloy decreased first and then increased, which were 8.1 μm (HE1), 6.3 μm (HE2) and 9.3 μm (HE3), respectively. And the uniformity of the alloy sheets microstructure could be roughly quantified by the standard deviation (S) of the Gaussian function (the smaller the S value, the more uniform the microstructure) (Ref 4). The S value were 3.6 μm (HE1), 2.7 μm (HE2) and 4.1 μm (HE3), respectively. This indicated that the microstructure uniformity of the alloy was expressively improved after extrusion (Ref 20). According to Zener–Hollomon parameters, when the extrusion temperature was constant, the strain rate increased as the ER
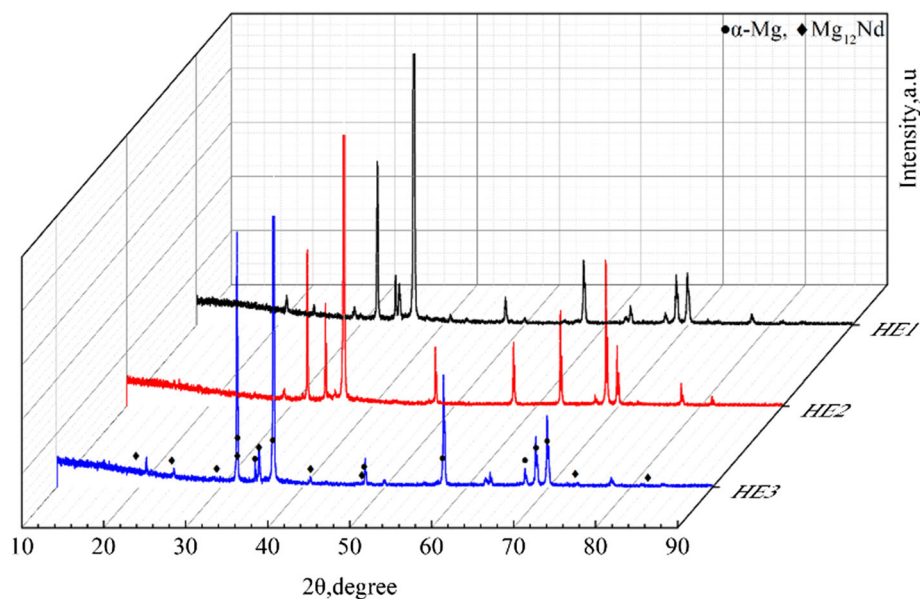

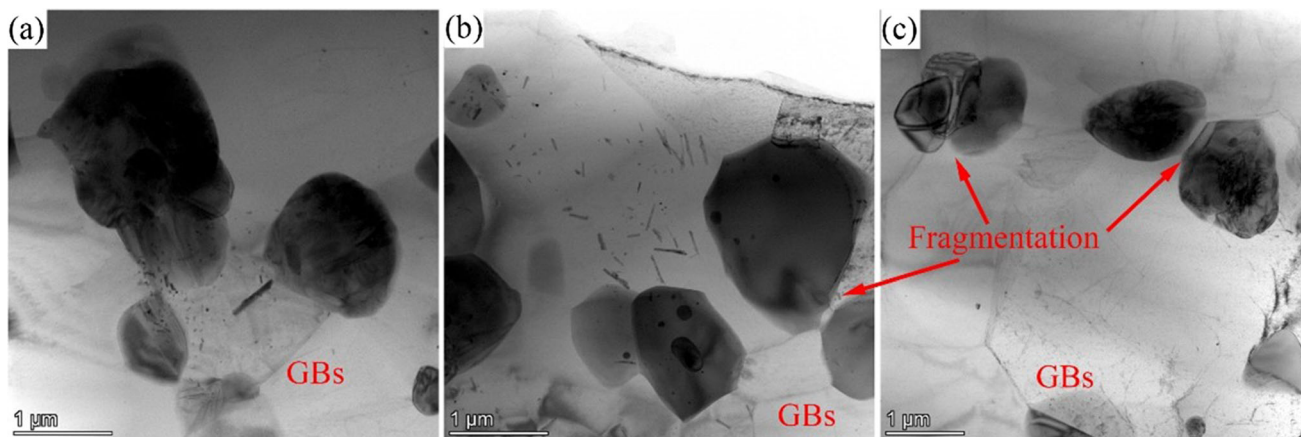**Fig. 3** XRD images of the Mg-2.5Nd-0.5Zn-0.5Zr alloy sheets

Fig. 4 TEM images of the Mg-2.5Nd-0.5Zn-0.5Zr alloy sheets: (a) HE1, (b) HE2, (c) HE3
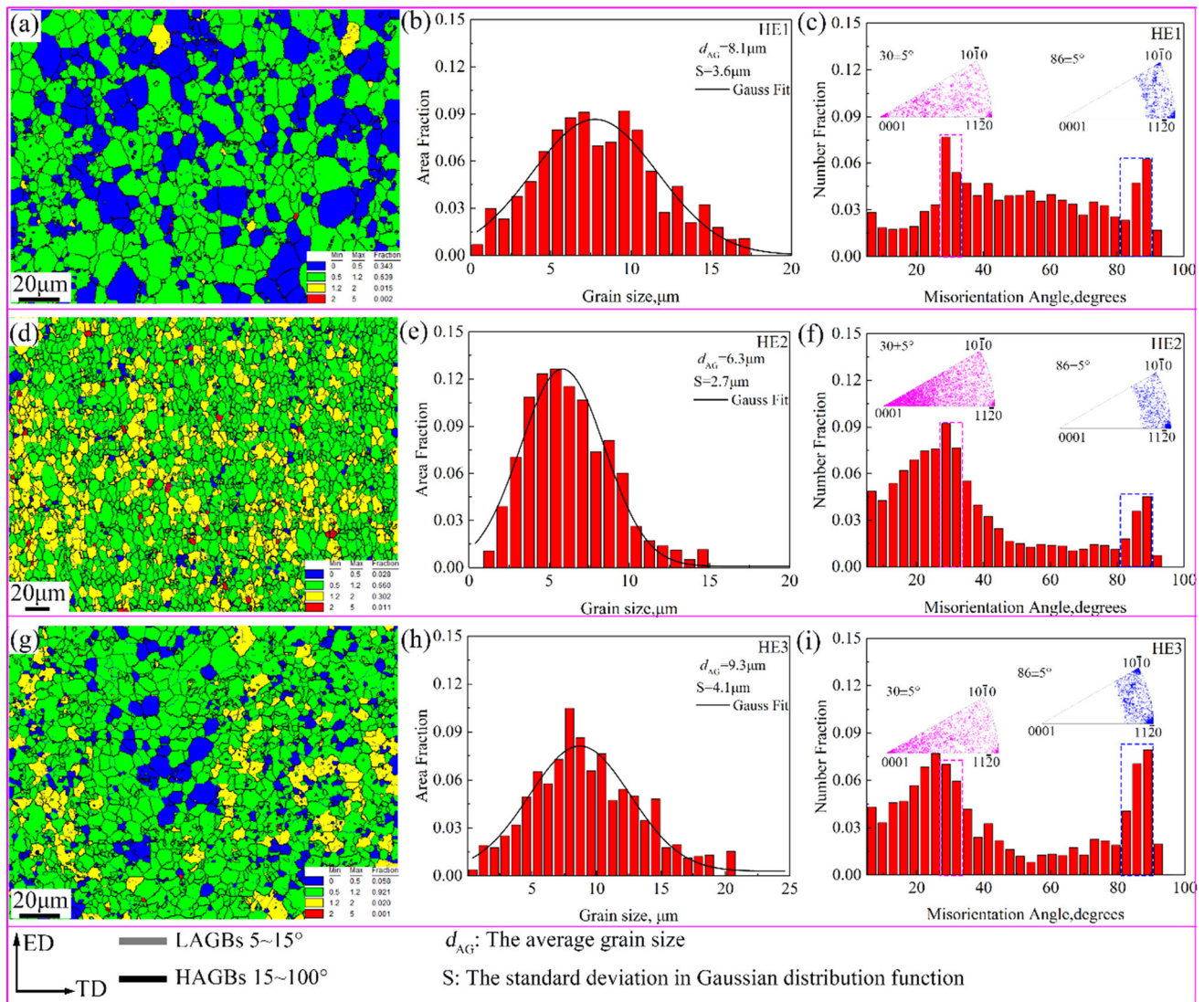
Fig. 5 Microstructure characteristics of the Mg-2.5Nd-0.5Zn-0.5Zr alloy sheets, (a, d, g) grain average misorientation, (b, e, h) grain size distribution, (c, f, i) misorientation angle

increased, the Z value was larger, and the dynamic recrystallized grain size was smaller (Ref 29). In fact, this work did not conform to this law. The reasons were as follows: When the ER was the largest (HE3), the deformation of the alloy was the most severe in the extrusion process and the deformation heat could not dissipate in time, resulting in the temperature of the extruded sheet was higher than the set extrusion temperature 400 °C. Therefore, the dynamic recrystallized grains of HE3 alloy sheet grew rapidly under the drove of temperature. For Mg alloys containing the second phase, PSN was also an important recrystallization mechanism (Ref 26, 27), which tended to generate large orientation gradient around larger particles due to deformation incoordination and high deformation storage energy, which was easy to trigger recrystallization nucleation. In Fig. 1 and 2 that there were a lot of coarse reticulated second phase in the initial alloy, and the average size of the broken second phase particles after extrusion deformation (HE1 and HE3) was greater than 1 μm. This means that PSN recrystallization might occurred during extrusion. Imandoust et al. (Ref 26) pointed out that continuous dynamic recrystallization usually occurred when the deformation tem-

perature was 300 ~ 450 °C. In this study, the extrusion temperature was 400 °C, indicated that continuous dynamic recrystallization was more likely to occur in the extrusion process. In addition, it can be seen from the figure that the change law of misorientation angle of the sheets after extrusion was basically consistent. During the extrusion process, the dislocations accumulated and rearranged at grain boundaries and severely deformed regions, forming low-angle grain boundaries. Low-angle grain boundaries absorbed dislocation to form recrystallization, which grew to form high-angle grain boundaries (Ref 30). Additionally, the misorientation angle of all the extruded sheets retained two peaks at 86.3 ± 5° and 30 ± 5°. The existence of these two peaks probably indicated two things: (1) The tension twinning participated in the extrusion deformation and formed a tension twinning boundary of 86.3°; (2) activation of prismatic slips and rotated crystal orientation around ⟨0001⟩about 30° during dynamic recrystallization process. This phenomenon has been reported in the studies of Imandoust et al. (Ref 27).

Figure 6 shows the kernel average misorientation (KAM) diagrams of the extruded sheets at different states. KAM

represents the geometrically necessary dislocations (GNDs) density distribution and orientation gradient in the grains. The ρ_{GNDS} could be expressed as (Ref 29): $\rho_{GNDS} = 2\Theta/\mu b$, where Θ is the average misorientation, b is the Burger vector (0.32 nm), u is the unite length of the point (equal to scan step size, 0.5, 0.8 μm). Θ is evaluated from the local misorientation profile in the KAM map (Fig. 6). According to the Θ values (0.592° (HE1), 1.001° (HE2) and 0.6084° (HE3)), the ρ_{GNDS} of HE1, HE2 and HE3 were about, 1.2924×10^{15} m^2, 1.3759×10^{15} m^2 and 1.326×10^{15} m^2, respectively. The driving force for dynamic recrystallization was the distortion energy difference between grains, which was determined by the dislocation density and its distribution. In Fig. 6, the distribution of local orientation deviation was not uniform, and the orientation deviation at grain boundary was generally higher than that inside grain. These results indicated that the dislocation accumulation at the grain boundary was severe and the deformation storage was large, which provided the power for the nucleation of the dynamic recrystallization. With the increase of extrusion ratio, the local misorientation deviation and dislocation density increased first and then decreased. And this change law was contrary to the proportion of dynamic recrystallization. (With the increase of extrusion ratio, the dynamic recrystallization proportion first decreased and then increased.) This indicated that dynamic recrystallization occurred at the expense of dislocation consumption during extrusion, this was consistent with the research results of Imandoust and Zhang et al. (Ref 26, 30).

3.3 Texture Characteristics

Figure 7 presents the pole figures and basal pole density of the alloy sheets. HE1 sheet showed weakened bimodal basal texture characteristics. (Maximum pole density was 6.7.) The preferred orientation of HE1 sheet in ED was obvious, the angle between grain c-axis and ED was mostly $60 \sim 80°$, while the texture in TD was diffuse. With the increase of ER, the texture strength of HE2 sheet increased obviously. (Maximum pole density was 15.8.) More importantly, the texture state also changed and showed a strong single-peak plate basal texture. The angle between grain c-axis and ED was concentrated among $60 \sim 90°$, and the angle between grain TD was concentrated among $70 \sim 90°$, both of which were in hard orientation. As the ER continued to increase, the texture of HE3 sheet was further strengthened, and the maximum pole density was 19.4. However, the texture state was greatly changed. The angle between grain c-axis and ED was concentrated among $30 \sim 70°$, and the angle between grain TD was also wider than

that of the first two sheets, because the grain orientation deviated from the hard orientation even closer to the soft orientation in the ED.

3.4 Mechanical Properties

Figure 8 displays the stress–strain curves of the alloys. It can be clearly seen from Fig. 8(a) that the initial alloy showed obvious isotropy in ED and TD. Along the ED, the yield strength (YS), ultimate tensile strength (UTS) and elongation (EL) were 112 ± 2 MPa, 212 ± 2 MPa and $21.6 \pm 1.2\%$, respectively. Along the TD, the YS, UTS and EL were 114 ± 3 MPa, 216 ± 4 MPa and $21.9 \pm 1.1\%$, respectively. After extrusion deformation, with the increase of the ER, the YS and UTS of the alloy in the ED and TD increased first and then decreased (Fig. 9). The YS_{TD} and UTS_{TD} were higher than those of the ED. The YS_{TD} was between 186 and 230 MPa and the UTS_{TD} was between 246 and 269 MPa. The YS_{ED} was between 126 and 215 MPa, and the UTS_{ED} was between 216 and 259 MPa. In addition, with the increase of ER, the anisotropy of the alloy decreased first and then increased. The EL in the ED of the alloy presented an increased trend, when the ER was the largest (HE3), the alloy exhibited excellent ductility (28.3%). In general, HE2 alloy showed excellent mechanical properties and low anisotropy. Specifically, ED: the YS, UTS and EL were 215 ± 2 MPa, 259 ± 3 MPa and $21.4 \pm 1.6\%$ respectively. TD: the YS, UTS and EL were 230 ± 4 MPa, 269 ± 2 MPa and $21.5 \pm 1.2\%$, respectively.

Generally speaking, the mechanical properties of the materials were mainly determined by their internal microstructure (such as second phase, grain size and texture state) (Ref 4, 30). It can be seen from Fig. 8 that the extrusion ratios have a significant effect on the mechanical properties of the alloy. First, Hall–Petch relationship was widely used to quantify the strengthening contribution from grain size. It can be learned from the Hall–Petch relationship that the yield strength increases as the grain size decreases (Ref 31):

$$\sigma_{0.2} = \sigma_0 + kd^{-1/2} \tag{Eq 1}$$

where σ_0 and k were material constants and d was the average grain size of the alloy. In Fig. 5, the microstructure of the extruded alloy sheets with different ERs was evenly distributed and the grain size distribution conformed to the Gaussian function distribution. In other words, the smaller the average grain size and the more uniform the distribution of the alloy, the higher the strength. Second, the second phases would pin the dislocations and impede the dislocation movement in Mg alloy according to the Orowan mechanism, thus strengthen Mg
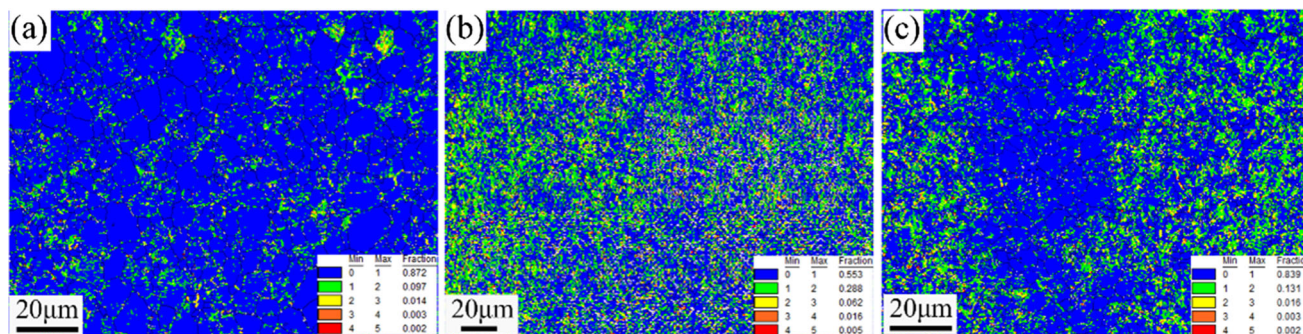

Fig. 6 Kernel average misorientation (KAM) maps of the Mg-2.5Nd-0.5Zn-0.5Zr alloy sheets, (a) HE1, (b) HE2, (c) HE3
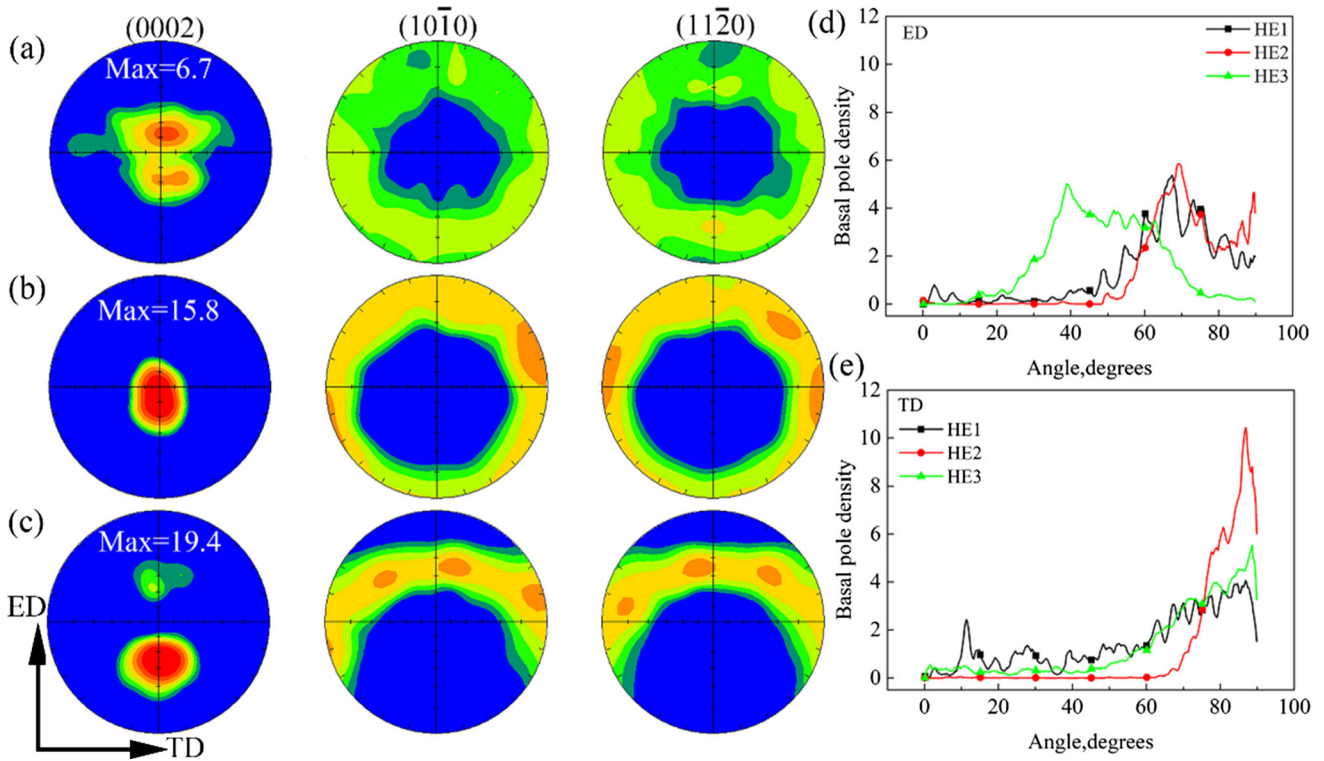
Fig. 7 (0002), (10-10) and (11-20) pole figures and basal pole density of the Mg-2.5Nd-0.5Zn-0.5Zr alloy sheets, (a) HE1, (b) HE2, (c) HE3, (d) ED, (e) TD

alloys. The precipitation strengthening can be written as follows (Ref 32):

$$\Delta\sigma_{PS} = M \frac{Gb}{2\pi\sqrt{1-v}} \frac{1}{\left(\sqrt{\frac{\pi}{4f}-1}\right)d_p} \ln\frac{d_p}{b} \qquad (Eq\ 2)$$

where M is the Taylor factor, v is the Poisson's ratio (0.35), G is the shear modulus (16.5 GPa), b is the Burger vector (0.32 nm), d_p is the average diameter of precipitates, f is the volume fraction of precipitates, according to the f and d_p in Table. 1. According to Eq 2, it can be calculated that the precipitation strengthening effect of these three alloys has the following relationship:

$$\Delta\sigma_{PS}(HE2) > \Delta\sigma_{PS}(HE3) > \Delta\sigma_{PS}(HE1)$$

Third, the dislocation strengthening contribution can be expressed as (Ref 33):

$$\Delta\sigma_{DS} = \alpha MGb\rho^{1/2} \qquad (Eq\ 3)$$

where α is a constant 0.2 and ρ is the geometrically necessary dislocations density (Fig. 6). According to Eq 3, it can be calculated that the dislocation strengthening effect of these three alloys has the following relationship:

$$\Delta\sigma_{DS}(HE2) > \Delta\sigma_{DS}(HE3) > \Delta\sigma_{DS}(HE1)$$

Finally, it is known that the basal slip would occur more easily in Mg alloys during room temperature deformation, while non-basal slips (prismatic slip and pyramidal slip) were hard to be activated (Ref 34, 35). Moreover, the Schmid factor of basal slip was directly determined by the crystallographic orientation of grain (Ref 36). When a grain was stretched perpendicular to the c-axis, the Schmid factor of basal slip of the grains with basal texture was 0, which means that the resolved shear stress of basal slip was 0 MPa, thus basal slip would not occur. The extruded alloys in the present study show strong basal texture, and most grains were subjected to tensile stress perpendicular to the c-axis during the tensile test along with ED. Therefore, the basal texture would prevent the activation of basal slip, thus cause texture strengthening in the Mg alloys. It can be seen from Fig. 7 that the texture strength of the alloy gradually increases with the increase of extrusion ratios. It can be concluded that the texture strengthening effect of HE3 alloy was more obvious than that of HE1 and HE2 alloy. Moreover, the average Schmid factor (m_{bas}) was obtained by EBSD data test, the ED m_{bas} values of HE, HE2 and HE3 alloys were 0.290536, 0.253249 and 0.418235, respectively, the TD m_{bas} values of HE1, HE2 and HE3 alloys were 0.251973, 0.227004 and 0.21495, respectively. It can be shown that when HE3 alloy was tensile along ED, the basal slip was easier to activated and the alloy has good plasticity. However, the strength of HE2 alloy was significantly higher than that of HE3 alloy, which indicated that refinement strengthening, precipitation strengthening and dislocation strengthening play a leading role. In conclusion, the combining strengthening effects of grain refinement, precipitation, dislocation and texture lead to that the YS and UTS of alloy HE2 are higher than those of alloy HE1 and HE3.

In our previous researches, the fiber basal texture sheet was easy to activate the basal slip and tensile twinning when stretched along the TD, resulting in smaller yield stress. In contrast, the multi-system slip needs to be activated to coordinate the deformation when stretched along the ED, resulting in larger yield strength and strong yield strength
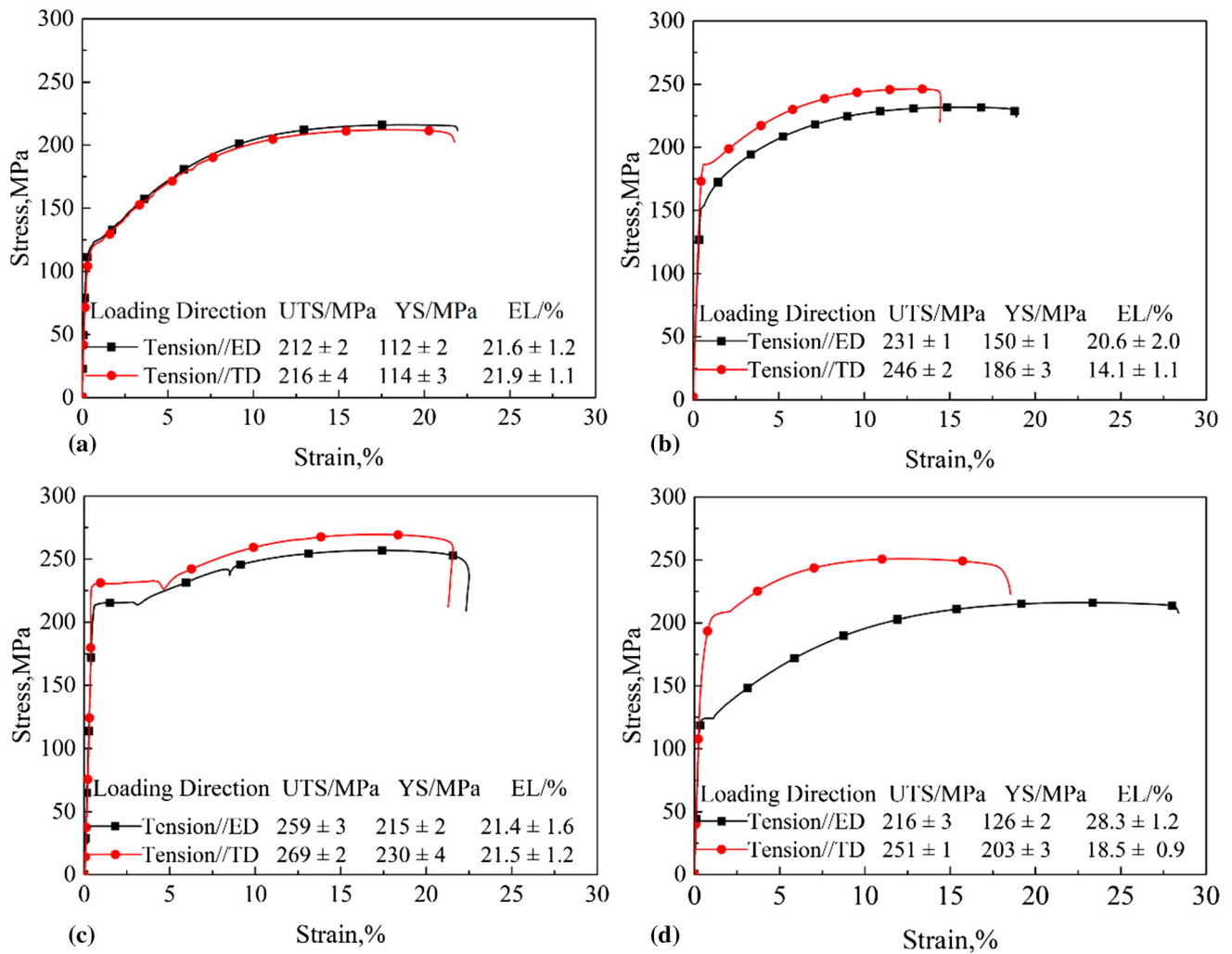
Fig. 8 Stress–strain curves of the Mg-2.5Nd-0.5Zn-0.5Zr alloys at different states, (a) Initial, (b) HE1, (c) HE2, (d) HE3
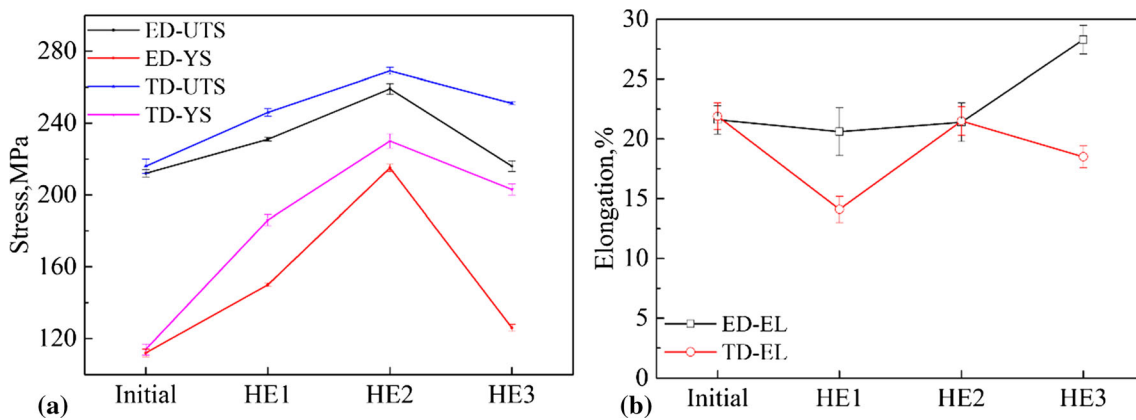

Fig. 9 Mechanical properties of the Mg-2.5Nd-0.5Zn-0.5Zr alloys, (a) stress, (b) elongation

anisotropy (Ref 37, 38). To explain the anisotropy of the alloy, crystal direction maps were used to characterize the deformation modes. In crystal orientation map, each point was identified based on the orientation relationship between a crystal direction and a sample direction. Activation of the deformation mechanism in Mg alloys depends largely on the frictional stress (σ_0) ($\sigma_0 = \tau_{CRSS}/m$, where τ_{CRSS} was the

critical resolved shear stress, and m was the average Schmid factor) (Ref 36, 39, 40). The results of Xin et al.(Ref 39, 40) show that when the critical resolved shear stress ratio of basal slip, tensile twinning and prismatic slip was 1:1:2, the dominant deformation mechanisms were tension twinning ($\theta = 0 \sim 23°$), basal slip ($\theta = 23 \sim 77°$) and prismatic slip ($\theta = 77 \sim 90°$), (θ refers to the angle between the loading direction and the normal

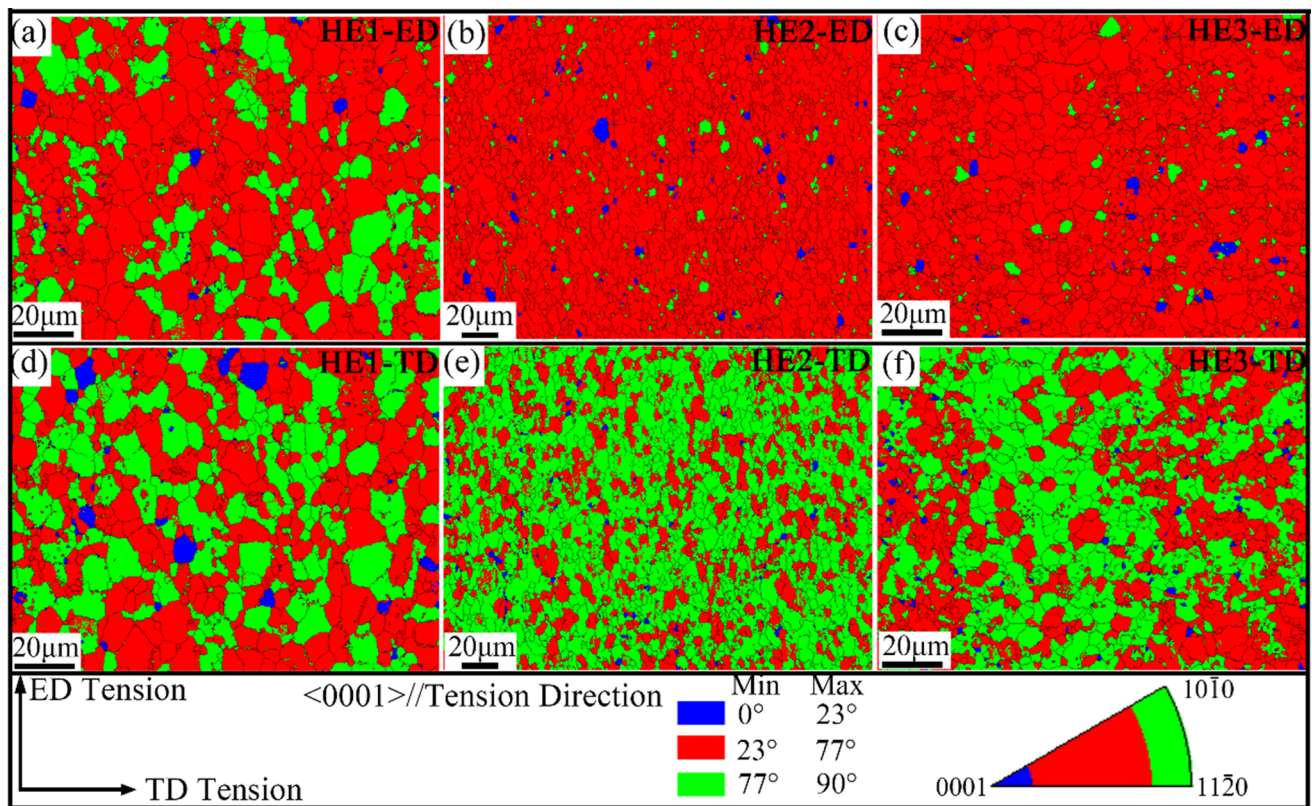**Fig. 10** Crystal direction map of the Mg-2.5Nd-0.5Zn-0.5Zr alloy sheets for different states. (In crystal direction map, the grains with ⟨0001⟩ away from the loading direction in the angle range of 0-23°, 23-77° and 77-90° are depicted by blue color, red color and green color, respectively) (Color figure online)

direction of the basal plane) (Ref 4, 39, 40). Combined with the angle distribution, the activation fraction of each deformation mode could be roughly estimated by the angle identification of each grain whose ⟨0001⟩met the above angle principle suggested by Xin. Figure 10 shows the tension direction (ED or TD) and ⟨0001⟩direction were selected as the sample direction and the crystal direction. In this work, the blue areas ($\theta = 0 \sim 23°$) were characterized as tension twinning, the red areas ($\theta = 23 \sim 77°$) were characterized by basal slip and the green areas ($\theta = 77 \sim 90°$) were characterized by prismatic slip. The corresponding activation fraction of each deformation mode is shown in Fig. 11. As can be seen, when the extruded sheets were tensile along the ED and TD, the fraction of tension twinning was less than 3%. (In Fig. 10, the number of blue grains was very small when tensile along the ED or TD.) Compared with basal slip and prismatic slip, its influence on deformation mechanism could be ignored. As can be seen from Fig. 10, with the increase of extrusion ratio in the resulting plates significantly increased the red grain number along the ED, whereas along the TD, the number of red particles decreases first and then increases, and the number of green particles increases first and then decreases. Finally, the number of red grain and green grain was basically the same. Correspondingly, the basal slip became the dominant deformation mode along the ED in the resulting plates but its fraction gradually increased with the increases of extrusion ratio (74.6% at HE1, 95.5% at HE2 and 95.7% at HE3 in Fig. 11a). Instead, the dominant deformation modes along the TD in the resulting plates were the prismatic ($40.4 \sim 66.7\%$) and basal slips

($32.4 \sim 56.7\%$) and their activation fractions were almost unchanged at different extrusion ratios (Fig. 11b).

In general, with the increase of ER, the proportion of basal slip increases gradually (74.6 to 95.5%) when the alloy was tensile in ED, and the deformation mechanism was mainly basal slip. When the alloy was tensile along the TD, the proportion of basal slip decreases gradually (56.7 to 32.4%), and the proportion of prismatic slip increases gradually (40.4 to 66.7). The main deformation mechanism was basal slip and prismatic slip.

4. Conclusions

(1) The dynamic recrystallization of Mg-2.5Nd-0.5Zn-0.5Zr alloy occurred during hot extrusion, and the microstructure was effectively refined. With the increase of ER, the basal texture changes from weak bimodal texture to strong basal texture with the texture strength increased significantly (from 6.7 to 19.4).

(2) With the increase of ER, the average grain size first decreased and then increased, while the change of the YS and UTS of the alloy was opposite. When the ER was 12.5, the alloy exhibited excellent mechanical properties. Specifically, ED: the YS, UTS and EL were 215 MPa, 259 MPa and 21.4%, respectively. TD: the YS, UTS and EL were 230 MPa, 269 MPa and 21.5%, respec-
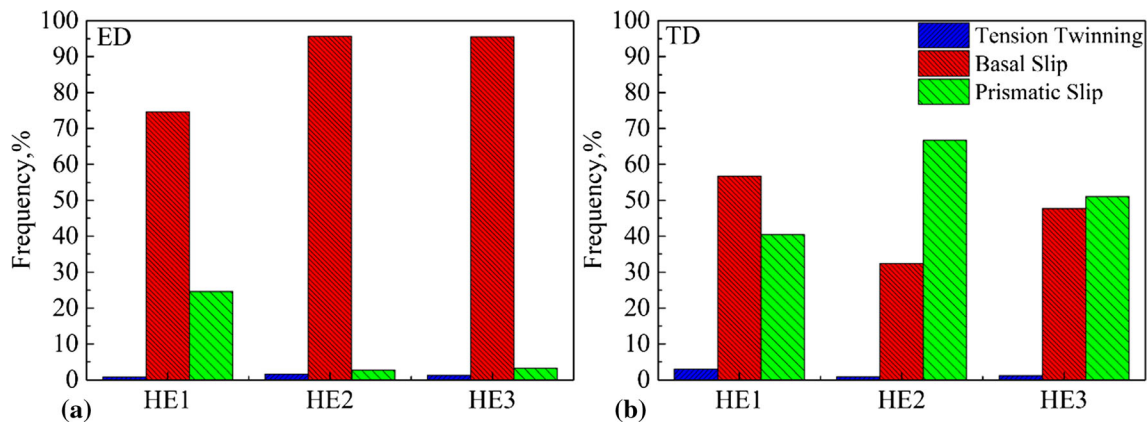
Fig. 11 Activation fraction of each deformation mode for the tension tests along the ED (a) and the TD (b) based on the orientation distribution in Fig. 10

tively. The higher strength results from the interaction of refinement strengthening, dislocation strengthening, precipitation strengthening and texture strengthening.

(3) With the increase of ER, the proportion of basal slip increased gradually when the alloy was tensile in ED, and the deformation mechanism was mainly basal slip. When the alloy was tensile along the TD, the proportion of basal slip decreased gradually, and the proportion of prismatic slip increased gradually. The main deformation mechanism was basal slip and prismatic slip.

Acknowledgments

References

1. J. Suh, J. Victoria-Hernández, D. Letzig, R. Golle, and W. Volk, Enhanced Mechanical Behavior and Reduced Mechanical Anisotropy of AZ31 Mg Alloy Sheet Processed by ECAP, *Mater. Sci. Eng. A*, 2016, **650**, p 523–529. https://doi.org/10.1016/j.msea.2015.09.058
2. X. Liu, H. Yang, B.W. Zhu, Y.Z. Wu, W.H. Liu, and C.P. Tang, Unveiling the Mechanical Response and Accommodation Mechanism of Pre-Rolled AZ31 Magnesium Alloy under High-Speed Impact Loading, *J. Magnes. Alloys*, 2022, **10**, p 1096–1108. https://doi.org/10.1016/j.jma.2021.07.030
3. S.W. Pan, Y.C. Xin, G.J. Huang, Q. Li, F.L. Guo, and Q. Liu, Tailoring the Texture and Mechanical Anisotropy of a Mg-2Zn-2Gd Plate by Varying the Rolling Path, *Mater. Sci. Eng. A*, 2016, **653**, p 93–98. https://doi.org/10.1016/j.msea.2015.12.002
4. W.Z. Chen, J.F. Ma, C. Cui, W.C. Zhang, W.K. Wang, X.T. Liu, J.L. Yang, and G.R. Cui, Texture Role in the Mechanical Property Improvement Contributed by Grain Refinement for Mg-26Nd-055Zn-05Zr Alloy Subjected to Extrusion Process, *Mater. Sci. Eng. A*, 2022, **831**, p 142185. https://doi.org/10.1016/j.msea.2021.142185
5. W.T. Sun, X.G. Qiao, M.Y. Zheng, C. Xu, S. Kamado, X.J. Zhao, H.W. Chen, N. Gao, and M.J. Starink, Altered Ageing Behaviour of a Nanostructured Mg-8.2Gd-3.8Y-1.0Zn-0.4Zr Alloy Processed by High Pressure Torsion, *Acta Mater.*, 2018, **151**, p 260–270. https://doi.org/10.1016/j.actamat.2018.04.003
6. B.S. Li, K. Guan, Q. Yang, X.D. Niu, D.D. Zhang, S.H. Lv, F.Z. Meng, Y.D. Huang, N. Hort, and J. Meng, Microstructures and Mechanical Properties of a hot-Extruded Mg-8Gd-3Yb-1.2Zn-0.5Zr (wt%) Alloy, *J. Alloys Compd.*, 2019, **776**, p 666–678. https://doi.org/10.1016/j.jallcom.2018.10.322
7. B.W. Zhu, X. Liu, C. Xie, J. Su, P.C. Guo, C.P. Tang, and W.H. Liu, Unveiling the Underlying Mechanism of Forming Edge Cracks Upon High Strain-Rate Rolling of Magnesium Alloy, *J. Mater. Sci. Technol.*, 2020, **50**, p 59–65. https://doi.org/10.1016/j.jmst.2020.03.006
8. Y. Xu, X.X. Zhang, W. Li, P.H. Hu, J.B. Jia, and J.T. Luo, Ultrafine Lamellar Structure AM60B Magnesium Alloy Sheet Prepared by High Strain Rate Rolling, *Mater. Sci. Eng. A*, 2020, **781**, p 139221. https://doi.org/10.1016/j.msea.2020.139221
9. J.R. Li, A.Y. Zhang, H.C. Pan, Y.P. Ren, Z.R. Zeng, Q.Y. Huang, C.L. Yang, L.F. Ma, and G.W. Qin, Effect of Extrusion Speed on Microstructure and Mechanical Properties of the Mg-Ca Binary Alloy, *J. Magnes. Alloys*, 2021, **9**(4), p 1297–1303. https://doi.org/10.1016/j.jma.2020.05.011
10. K. Guan, R. Ma, J.H. Zhang, R.Z. Wu, Q. Yang, and J. Meng, Modifying Microstructures and Tensile Properties of Mg-Sm Based Alloy Via Extrusion Ratio, *J. Magnes. Alloys*, 2021, **9**, p 1098–1109. https://doi.org/10.1016/j.jma.2020.12.004
11. H. Lv, L. Li, Z.Z. Wen, C.R. Liu, W. Zhou, X. Bai, and H.L. Zhong, Effects of Extrusion Ratio and Temperature on the Microstructure and Mechanical Properties of Mg-Zn-Yb-Zr Extrusion Alloys, *Mater. Sci. Eng., A*, 2022, **833**, p 142521. https://doi.org/10.1016/j.msea.2021.142521
12. S.Y. Lyu, W.L. Xiao, R.X. Zheng, F. Wang, T. Hu, and C.L. Ma, Fabrication of High-Strength Mg-Y-Sm-Zn-Zr Alloy by Conventional Hot Extrusion and Aging, *Mater. Sci. Eng. A*, 2018, **732**, p 178–185. https://doi.org/10.1016/j.msea.2018.06.085
13. Z.Z. Gui, Z.X. Kang, and Y.Y. Li, Evolution of the Microstructure and Fracture Characteristics of a Mg-Nd-Zn-Zr-Mn Alloy Through Heat Treatment and Extrusion, *J. Alloy. Compd.*, 2018, **765**, p 470–479. https://doi.org/10.1016/j.jallcom.2018.06.185
14. P.H. Fu, L.M. Peng, H.Y. Jiang, J.W. Chang, and C.Q. Zhai, Effects of Heat Treatments on the Microstructures and Mechanical Properties of Mg-3Nd-0.2Zn-0.4Zr (wt.%) Alloy, *Mater. Sci. Eng. A*, 2008, **486**, p 183–192. https://doi.org/10.1016/j.msea.2007.08.064
15. L. Ma, R.K. Mishra, M.P. Balogh, L.M. Peng, A.A. Luo, A.K. Sachdev, and W.J. Ding, Effect of Zn on the Microstructure Evolution of Extruded Mg-3Nd (-Zn)-Zr (wt.%) Alloys, *Mater. Sci. Eng. A*, 2012, **543**, p 12–21. https://doi.org/10.1016/j.msea.2012.02.030
16. A.R. Natarajan, E.L.S. Solomon, B. Puchala, E.A. Marquis, and A.V. Ven, On the Early Stages of Precipitation in Dilute Mg-Nd Alloys, *Acta Mater.*, 2016, **108**, p 367–379. https://doi.org/10.1016/j.actamat.2016.01.055
17. E.L.S. Solomon, V. Araullo-Peters, J.E. Allison, and E.A. Marquis, Early Precipitate Morphologies in Mg-Nd-(Zr) Alloys, *Scripta Mater.*, 2017, **128**, p 14–17. https://doi.org/10.1016/j.scriptamat.2016.09.015
18. Z.J. Yu, C. Xu, J. Meng, K. Liu, J.L. Fu, and S. Kamado, Effects of Extrusion Ratio and Temperature on the Mechanical Properties and Microstructure of as-Extruded Mg-Gd-Y-(Nd/Zn)-Zr Alloys, *Mater. Sci. Eng. A*, 2019, **762**, p 138080. https://doi.org/10.1016/j.msea.2019.138080

19. J.D. Robson, A.M. Twier, G.W. Lorimer, and P. Rogers, Effect of Extrusion Conditions on Microstructure, Texture, and Yield Asymmetry in Mg-6Y-7Gd-0.5 wt.%Zr Alloy, *Mater. Sci. Eng. A*, 2011, **528**, p 7247–7256. https://doi.org/10.1016/j.msea.2011.05.075

20. Y.J. Chen, Q.D. Wang, J.G. Peng, C.Q. Zhai, and W.J. Ding, Effects of Extrusion Ratio on the Microstructure and Mechanical Properties of AZ31 Mg Alloy, *J. Mater. Process. Technol.*, 2007, **182**, p 281–285. https://doi.org/10.1016/j.jmatprotec.2006.08.012

21. M. Shahzad and L. Wagner, Influence of Extrusion Parameters on Microstructure and Texture Developments, and their Effects on Mechanical Properties of the Magnesium Alloy AZ80, *Mater. Sci. Eng., A*, 2009, **506**, p 141–147. https://doi.org/10.1016/j.msea.2008.11.038

22. K. Hagihara, Z.X. Li, M. Yamasaki, Y. Kawamura, and T. Nakano, Strengthening Mechanisms Acting in Extruded Mg-Based Long-Period Stacking Ordered (LPSO)-Phase Alloys, *Acta Mater.*, 2019, **163**, p 226–239. https://doi.org/10.1016/j.actamat.2018.10.016

23. W.Q. Tang, S.Y. Huang, S.R. Zhang, D.Y. Li, and Y.H. Peng, Influence of Extrusion Parameters on Grain Size and Texture Distributions of AZ31 Alloy, *J. Mater. Process. Technol.*, 2011, **211**, p 1203–1209. https://doi.org/10.1016/j.jmatprotec.2011.01.014

24. S.H. Wang, W.C. Zhang, J.L. Yang, J.Q. Pan, H.X. Wang, W.Z. Chen, and G.R. Cui, Evolution of Microstructures, Texture, Damping and Mechanical Properties of Hot Extruded Mg-Nd-Zn-Zr Alloy, *J. Mater. Eng. Perform.*, 2021, **30**, p 8872–8882. https://doi.org/10.1007/s11665-021-06134-z

25. C.D. Barrett, A. Imandoust, A.L. Oppedal, K. Inal, M.A. Tschopp, and H.E. Kadiri, Effect of Grain Boundaries on Texture Formation During Dynamic Recrystallization of Magnesium Alloys, *Acta Mater.*, 2017, **128**, p 270–283. https://doi.org/10.1016/j.actamat.2017.01.063

26. A. Imandoust, C.D. Barrett, T. Al-Samman, K.A. Inal, and H. El Kadiri, A Review on the Effect of Rare-Earth Elements on Texture Evolution During Processing of Magnesium Alloys, *J. Mater. Sci.*, 2017, **52**, p 1–29. https://doi.org/10.1007/s10853-016-0371-0

27. A. Imandoust, C.D. Barrett, A.L. Oppedal, W.R. Whittington, Y. Paudel, and H.E. Kadiri, Nucleation and Preferential Growth Mechanism of Recrystallization Texture in High Purity Binary Magnesium-Rare Earth Alloys, *Acta Mater.*, 2017, **138**, p 27–41. https://doi.org/10.1016/j.actamat.2017.07.038

28. W.K. Wang, W.Z. Chen, W.Z. Zhang, G.R. Cui, and E.D. Wang, Weakened Anisotropy of Mechanical Properties in Rolled ZK60 Magnesium Alloy Sheets with Elevated Deformation Temperature, *J. Mater. Sci. Technol.*, 2018, **34**, p 2042–2050. https://doi.org/10.1016/j.jmst.2018.02.019

29. S.H. Wang, W.C. Zhang, H.X. Wang, J.L. Yang, W.Z. Chen, G.R. Cui, and G.F. Wang, Microstructures Evolution, Texture Characteristics and Mechanical Properties of Mg-2.5Nd-0.5Zn-0.5Zr Alloy During the High Strain Rate Hot-Rolling, *Mater. Sci. Eng. A*, 2021, **803**, p 140488. https://doi.org/10.1016/j.msea.2020.140488

30. Q. Zhang, Q.N. Li, X.Y. Chen, J.X. Zhao, J. Bao, and Z.Y. Chen, Dynamic Precipitation and Recrystallization Mechanism During Hot Compression of Mg-Gd-Y-Zr Alloy, *J. Market. Res.*, 2021, **15**, p 37–51. https://doi.org/10.1016/j.jmrt.2021.08.013

31. W. Yuan, S.K. Panigrahi, J.Q. Su, and R.S. Mishra, Influence of Grain Size and Texture on Hall-Petch Relationship for a Magnesium Alloy, *Scripta Mater.*, 2011, **65**, p 994–997. https://doi.org/10.1016/j.scriptamat.2011.08.028

32. J.F. Nie, Effects of Precipitate Shape and Orientation on Dispersion Strengthening in Magnesium Alloys, *Scripta Mater.*, 2003, **48**, p 1009–1015. https://doi.org/10.1016/S1359-6462(02)00497-9

33. H. Pan, R. Kang, J. Li, H. Xie, Z. Zeng, Q. Huang, C. Yang, Y. Ren, and G. Qin, Mechanistic Investigation of a Low-Alloy Mg–Ca-Based Extrusion Alloy with High Strength-Ductility Synergy, *Acta Mater.*, 2020, **186**, p 278–290. https://doi.org/10.1016/j.actamat.2020.01.017

34. B.N. Du, Z.Y. Hu, L.Y. Sheng, D.K. Xu, Y.X. Qiao, B.J. Wang, J. Wang, Y.F. Zheng, and T.F. Xi, Microstructural Characteristics and Mechanical Properties of the Hot Extruded Mg-Zn-Y-Nd Alloys, *J. Mater. Sci. Technol.*, 2021, **60**, p 44–55. https://doi.org/10.1016/j.jmst.2020.05.021

35. P.C. Guo, X. Liu, B.W. Zhu, W.H. Liu, and L.Q. Zhang, The Microstructure Evolution and Deformation Mechanism in a Casting AM80 Magnesium Alloy under Ultra-High Strain Rate Loading, *J. Magnes. Alloys*, 2021 https://doi.org/10.1016/j.jma.2021.07.032

36. Y. Wang and H. Choo, Influence of Texture on Hall-Petch Relationships in an Mg Alloy, *Acta Mater.*, 2014, **81**, p 83–97. https://doi.org/10.1016/j.actamat.2014.08.023

37. W. Wang, W. Chen, W. Zhang, G. Cui, and E. Wang, Effect of Deformation Temperature on Texture and Mechanical Properties of ZK60 Magnesium Alloy Sheet Rolled by Multi-Pass Lowered-Temperature Rolling, *Mater. Sci. Eng. A*, 2018, **712**, p 608–615. https://doi.org/10.1016/j.msea.2017.12.024

38. L. Zhang, W. Chen, W. Zhang, W. Wang, and E. Wang, Microstructure and Mechanical Properties of thin ZK61 Magnesium Alloy Sheets by Extrusion and Multi-Pass Rolling with Lowered Temperature, *J. Mater. Process. Technol.*, 2016, **237**, p 65–74. https://doi.org/10.1016/j.jmatprotec.2016.06.005

39. B. Guan, Y. Xin, X. Huang, P. Wu, and Q. Liu, Quantitative Prediction of Texture Effect on Hall-Petch Slope for Magnesium Alloys, *Acta Mater.*, 2019, **173**, p 142–152. https://doi.org/10.1016/j.actamat.2019.05.016

40. H. Yu, Y. Xin, M. Wang, and Q. Liu, Hall-Petch Relationship in Mg Alloys: A Review, *J. Mater. Sci. Technol.*, 2018, **34**, p 248–256. https://doi.org/10.1016/j.jmst.2017.07.022